Cell Reports

Article

A WW Tandem-Mediated Dimerization Mode of SAV1 Essential for Hippo Signaling

Graphical Abstract

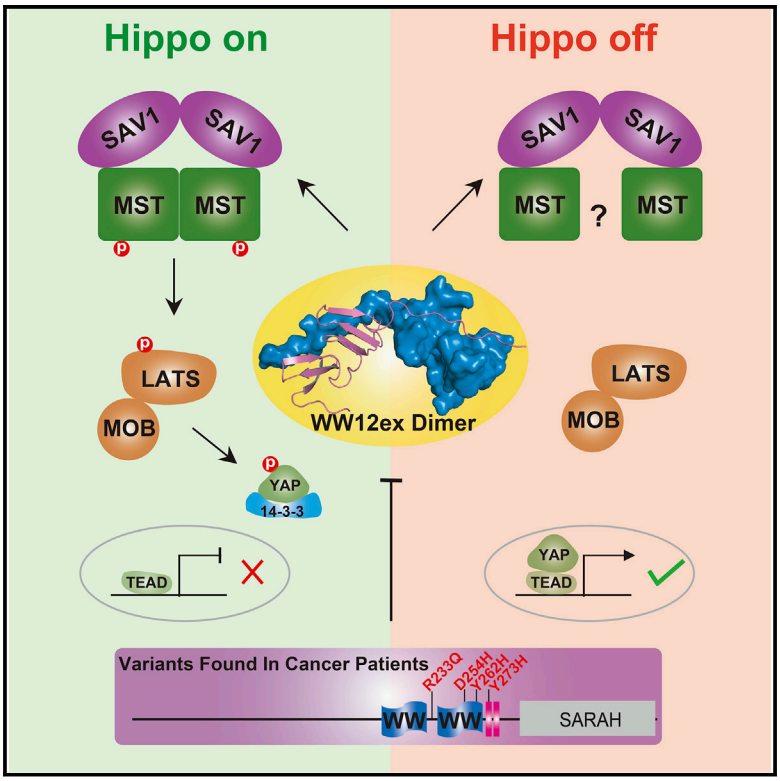

Highlights

- SAV1 WW tandem binds to a short sequence following the tandem and forms a stable dimer
- The extension sequence binds both WW domains via the type I PY-motif binding mode
- Disruption of WW-tandem-mediated SAV1 dimer impairs SAV1/MST complex formation
- Multiple SAV1 cancer variants are defective in WW tandem-mediated dimer formation

Authors

Zhijie Lin, Ruiling Xie, Kunliang Guan, Mingjie Zhang

Correspondence

mzhang@ust.hk

In Brief

Lin et al. report the crystal structure of the SAV1 WW12 tandem dimer, showing that the proline-rich tail following the WW tandem governs domain-swapped SAV1 dimer formation. WW tandem-mediated SAV1 dimer formation is important for the interaction between SAV1 and MST during Hippo signaling.

Lin et al., 2020, Cell Reports *32*, 108118
September 8, 2020
https://doi.org/10.1016/j.celrep.2020.108118

CellPress

Cell Reports

CellPress
OPEN ACCESS

Article

A WW Tandem-Mediated Dimerization Mode of SAV1 Essential for Hippo Signaling

Zhijie Lin,[1] Ruiling Xie,[2,3] Kunliang Guan,[2] and Mingjie Zhang[1,4,5,*]

[1]Division of Life Science, State Key Laboratory of Molecular Neuroscience, Hong Kong University of Science and Technology, Clear Water Bay, Kowloon, Hong Kong, China

[2]Department of Pharmacology and Moores Cancer Center, University of California, San Diego, La Jolla, CA 92093, USA

[3]Department of Otolaryngology, Head & Neck Surgery, Peking University First Hospital, Beijing 100034, China

[4]Center of Systems Biology and Human Health, Hong Kong University of Science and Technology, Clear Water Bay, Kowloon, Hong Kong, China

[5]Lead Contact

*Correspondence: mzhang@ust.hk

https://doi.org/10.1016/j.celrep.2020.108118

SUMMARY

The canonical mammalian Hippo pathway contains a core kinase signaling cascade requiring upstream MST to form a stable complex with SAV1 in order to phosphorylate the downstream LATS/MOB complex. Though SAV1 dimerization is essential for the trans-activation of MST, the molecular mechanism underlying SAV1 dimerization is unclear. Here, we discover that the SAV1 WW tandem containing a short Pro-rich extension immediately following the WW tandem (termed as "WW12ex") forms a highly stable homodimer. The crystal structure of SAV1 WW12ex reveals that the Pro-rich extension of one subunit binds to both WW domains from the other subunit. Thus, SAV1 WW12ex forms a domain-swapped dimer instead of a WW2 homodimerization-mediated dimer. The WW12ex-mediated dimerization of SAV1 is required for the MST/SAV1 complex assembly and MST kinase activation. Finally, we show that several cancer-related *SAV1* variants disrupt SAV1 dimer formation, and thus, these mutations may impair the tumor-suppression activity of SAV1.

INTRODUCTION

The Hippo signaling pathway is evolutionarily conserved and critical for organ size control and tissue homeostasis. In mammals, the canonical Hippo pathway contains a core kinase cascade, in which the MST (mammalian STE20-like protein kinase)/SAV1 (Salvador homolog 1) complex phosphorylates and activates the LATS (large tumor suppressor homolog proteins)/MOB (Mps one binder proteins) complex. The activated LATS kinases then phosphorylate and sequester YAP/TAZ transcription factors in cytoplasm, thereby turning off their transcriptional activities (Pan, 2010; Yu et al., 2015; Sun and Irvine, 2016; Fulford et al., 2018; Moya and Halder, 2019).

SAV1 is a scaffold protein that contains an N-terminal flexible region capable of binding to Merlin/NF2 and the striatin-interacting phosphatase and kinase complex (STRIPAK), a middle WW domain tandem capable of dimerization but with an unclear or debatable mechanism, and a C-terminal SARAH (Salvador-RassF-Hippo) domain that can heterodimerize with the SARAH domain of MST1/2 (Yu et al., 2010; Bae et al., 2017; Ohnishi et al., 2007; Pantalacci et al., 2003; Callus et al., 2006; Cairns et al., 2018). Formation of the MST/SAV1 complex and subsequent activation of MST kinases require interaction between the SARAH domains of the two proteins as well as SAV1 self-association (Callus et al., 2006; Bae et al., 2017). Previous biochemical and nuclear magnetic resonance structural studies have suggested that SAV1 self-association is mediated by its WW2-mediated formation of a weak homodimer (Ohnishi et al., 2007; Bae et al., 2017). We show in this study that the WW2-mediated dimerization is likely not a key mechanism for the SAV1 homodimer formation.

WW-domain-mediated target binding has been extensively studied (Sudol and Hunter, 2000; Salah et al., 2012). Accordingly, a number of putative targets, including LATS/Warts, angiomotins (AMOTs), AKT1, and RUNX, have been reported to bind to the WW domains of SAV1 via the canonical WW/"PPxY" motif (or PY motif in short) interaction mode (Tapon et al., 2002; Mana-Capelli and McCollum, 2018; Jiang et al., 2019; Min et al., 2012; Won et al., 2019). Many of the above-mentioned studies used individual WW domains or truncated WW12 tandem of SAV1 for binding assays. In our hands, using highly purified proteins, we could hardly detect any binding of the SAV1 WW tandem to the tandem PY-motif-containing proteins, including LATS1/2, AMOTs, PTPN14, and PTPN21 (Lin et al., 2019). Our finding is corroborated by the proteomic studies searching for SAV1-binding proteins by other groups (Hauri et al., 2013; Kwon et al., 2013; Wang et al., 2014; Vargas et al., 2020). Recently, we demonstrated that the WW-domain-containing proteins (e.g., KIBRA, YAP, MAGI2, and MAGI3) involved in cell growth and polarity use their WW tandems to bind to specific targets containing multiple PY motifs. Such WW-tandem-mediated

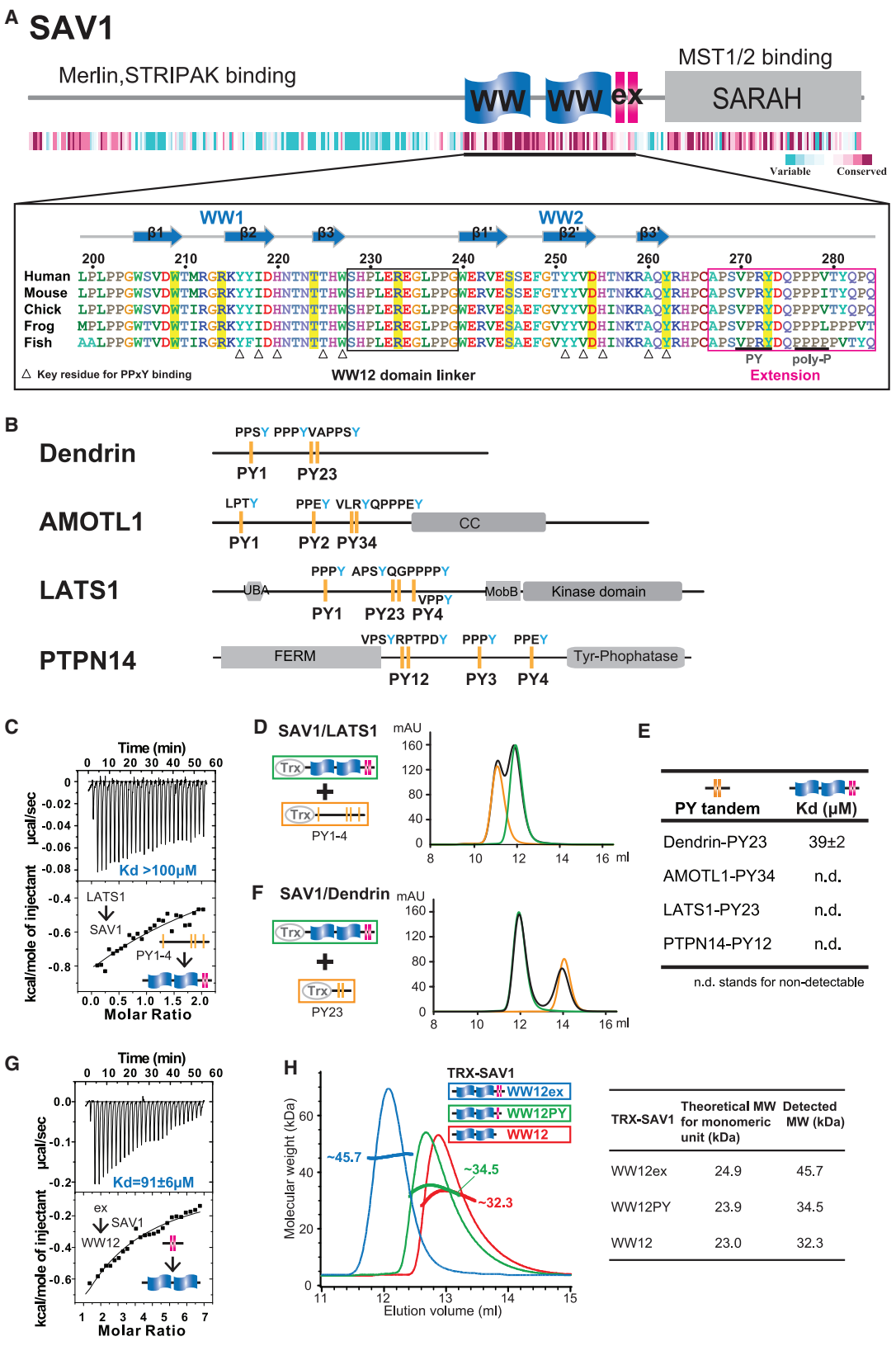

(legend on next page)

target interactions allow formation of very stable and highly specific WW domain protein/target complexes required for cell growth and signaling (Ji et al., 2019; Lin et al., 2019). The WW-tandem-mediated target recognition has also been reported in other multiple WW domain proteins, such as HECT family E3 ubiquitin ligases (Chong et al., 2010). Like other WW tandem proteins involved in cell growth, SAV1 also contains two WW domains connected by a completely conserved 12-residue sequence (Figure 1A). We hypothesized that the evolutionally conserved WW12 tandem of SAV1, like the WW tandems of KIBRA, YAP, and MAGIs, may also function as an integral unit in binding to its targets that are still to be discovered.

Deregulation of the Hippo pathway has been linked to a wide range of human cancers (Yu et al., 2015; Ma et al., 2019; Zheng and Pan, 2019). Consistent with the critical roles of SAV1 in the Hippo pathway, genomic copy number loss of *SAV1* or downregulation of SAV1 protein level is known to be associated with different types of human cancers, such as high-grade clear cell renal cell carcinoma (ccRCC), colorectal cancer, pancreatic ductal adenocarcinoma (PDAC), mucinous tubular and spindle cell carcinoma, and hepatocellular carcinoma (Matsuura et al., 2011; Mehra et al., 2016; Sohn et al., 2016; Wang et al., 2016; Jiang et al., 2017). Mining the catalogue of somatic mutations in cancer (COSMIC) database (https://cancer.sanger.ac.uk/cosmic) identifies many variants within the WW tandem of SAV1 in patients with cancers (see below for detail). Detailed biochemical and structural studies of the SAV1 WW tandem may shed light on the molecular mechanism underlying the MST/SAV1 complex assembly and offer insights into the potential impacts of the cancer-related SAV1 variants on the Hippo pathway activity.

In this study, we tested our hypothesis that the SAV1 WW12 tandem may function as an integral structural and functional unit in the Hippo pathway using combined biochemical and structural biology approaches. We discovered that a highly conserved Pro-rich sequence extension immediately following SAV1 WW2 directly binds to the WW12 tandem, forming a stable domain-swapped dimer. This domain-swapped SAV1 dimer formation is critical for the MST/SAV1 complex assembly and the Hippo pathway activation. Thus, our study reveals molecular insights into the scaffolding role of SAV1 in the Hippo core kinase cascade.

RESULTS

WW12ex, but Not WW12, of SAV1 Forms a Stable Dimer

SAV1 and LATS/Warts have been reported to interact with each other via direct binding between the WW domains of SAV1 and the PY-motifs of LATS/Warts (Tapon et al., 2002; Ni et al., 2015). A quantitative binding study showed that SAV1 WW domains binds to the PY1 motif of LATS1 with a dissociation constant (K_d) of ~150 μM (Ni et al., 2015). Such a weak binding is likely not adequate for SAV1 to organize its targets with sufficient specificity and stability (Ji et al., 2019; Lin et al., 2019). We then tested whether multiple PY motifs together might render LATS1 to bind to the SAV1 WW tandem with high affinity, like the interactions of LATS1 PY23 to the tandem WW domains of KIBRA, MAGI2, and MAGI3 (Lin et al., 2019). We purified a highly conserved SAV1 fragment containing its WW12 tandem and a highly conserved extension sequence immediately following WW12 (residues E198–Q285 in mouse SAV1 and termed as SAV1 WW12ex; Figure 1A) and a fragment of LATS1 containing all four PY motifs (PY1–4 covering residues N361–E582; Figure 1B). Isothermal titration calorimetry (ITC)-based assay only detected a very weak binding between SAV1 WW12ex and LATS1 PY1–4 (K_d > 100 μM; Figure 1C). This weak interaction was further verified by size-exclusion chromatography showing that mixing of the equal molar amount of SAV1 WW12ex and LATS1 PY1–4 did not cause obvious elution volume changes of either protein (Figure 1D).

Like the WW tandems from KIBRA and MAGIs (Lin et al., 2019), the two WW domains of SAV1 are connected by a short (12 residues) and completely conserved linker sequence (Figure 1A). Thus, we further tested whether the SAV1 WW tandem, analogous to the WW tandems of KIBRA and MAGIs, could selectively bind to two PY motifs separated by only 2 to 3 residues (Ji et al., 2019; Lin et al., 2019). Disappointedly, there were no detectable interactions between SAV1 WW12ex and the PY motif repeats from AMOTL1 PY34, LATS1 PY23, and PTPN14 PY12 (Figures 1B, 1E, and S1). A very weak interaction (K_d ~39 μM, an affinity typical for many single WW domain/PY motif interactions) was detected between dendrin PY23 and SAV1 WW12ex (Figures 1E and S1A). This is in sharp contrast to the very strong bindings (K_d values of a few nM) of dendrin PY23 to WW tandems of

Figure 1. Dimerization of SAV1 WW12ex

(A) Schematic diagram showing the domain organization of SAV1. The heatmap below the scheme shows the amino acid sequence conservation of SAV1 throughout the evolution. The amino acid sequences of SAV1 WW12ex from different species are aligned at the bottom of the panel. Key residues for the "PPxY" motif binding are denoted with triangles. Variants found in patients with caners are shaded in yellow.

(B) Schematic diagram showing the domain organization of selected multiple PY-motif-containing proteins in cell growth and polarity.

(C) ITC-based measurement of the binding of SAV1 WW12ex to LATS1 PY1–4.

(D) The analytical gel filtration chromatography elution profiles of SAV1 WW12ex (green), LATS1 PY1–4 (gold), and their mixture (black) with each protein at a concentration of 50 μM.

(E) ITC-derived binding affinities of SAV1 WW12ex to various closely spaced PY motif repeats shown in (B).

(F) The analytical gel filtration chromatography elution profiles of SAV1 WW12ex (green), dendrin PY23 (gold), and their mixture (black) with each protein at a concentration of 50 μM.

(G) ITC-based measurement showing the weak interaction between WW12 and the extension sequence of SAV1.

(H) Analytical gel filtration chromatography coupled with static light scattering analysis showing that SAV1 WW12ex forms a stable dimer in solution. Truncating the poly-P or both poly-P motif and PY motif impairs the dimer formation of SAV1 WW12ex. WW12ex (aas E198–Q285), WW12PY (aas E198–Q276), and WW12 (aas E198–A268) are colored in blue, green, and red, respectively.

K_d values of the ITC assays here and below are reported as fitted result ± fitting error of the corresponding experimental binding curve. Also see Figure S1.

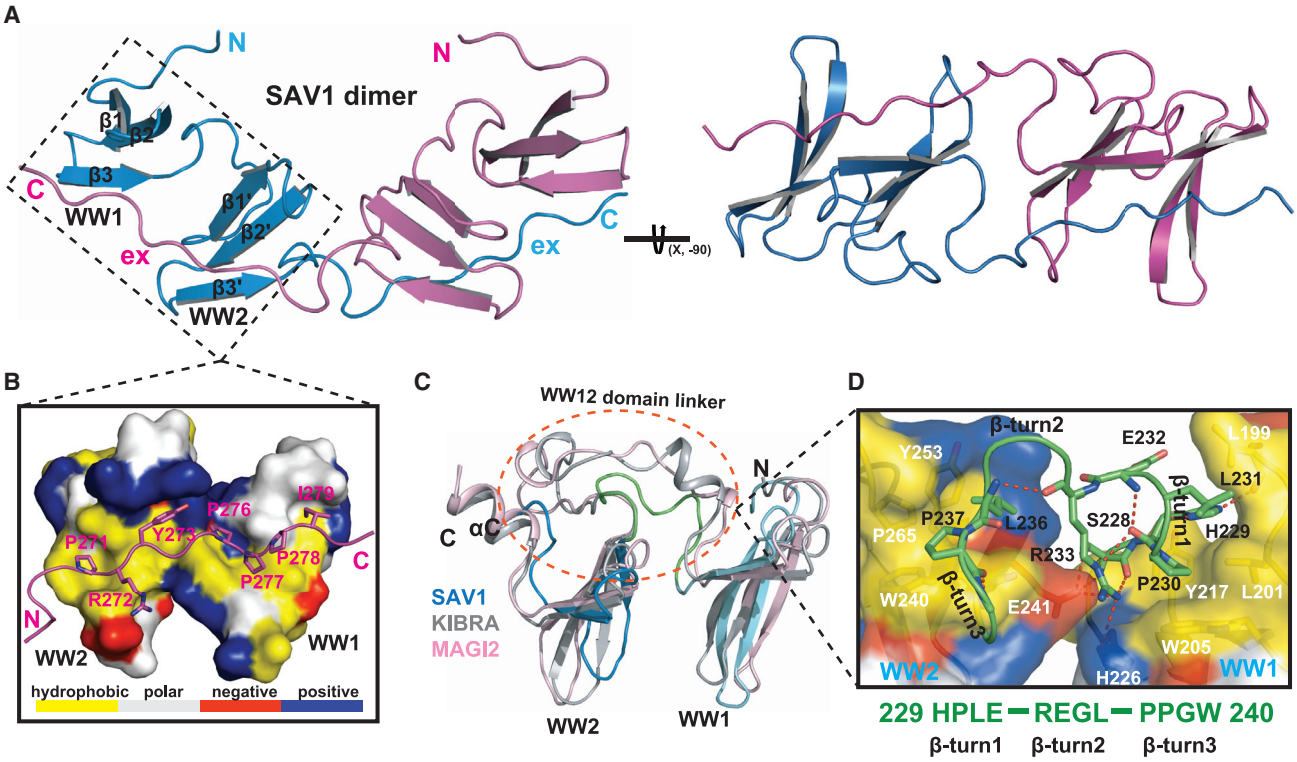

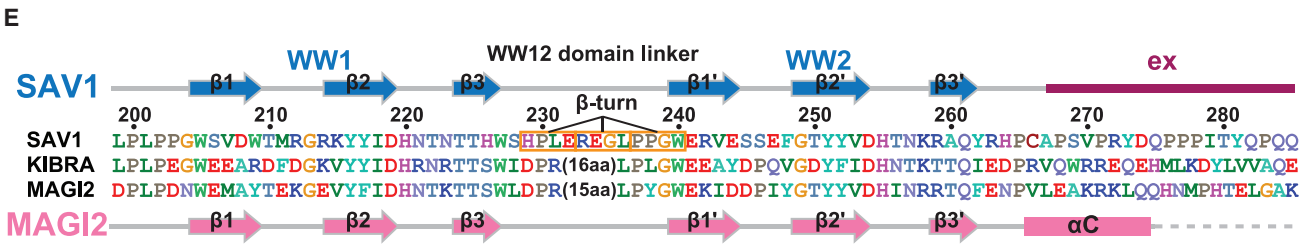

Figure 2. Crystal Structure of the SAV1 WW12ex Homodimer

(A) Ribbon diagram showing the overall structure of the SAV1 WW12ex dimer.

(B) Surface combined with ribbon-stick model showing the interaction between WW12 and the extension in SAV1. Residues in WW12 that are hydrophobic, negatively charged, and positively charged are colored in yellow, red, and blue, respectively.

(C) Superimposition of the structures of the WW tandems from SAV1, KIBRA (PDB: 6J69), and MAGI2 (PDB: 6JJZ), each in complex with their respective targets.

(D) Combined surface and ribbon-stick model showing the structural basis for the coupling of the two WW domains by the 12-residue linker in SAV1. The 12-residue linker forms 3 continuous β-turns and is colored in green.

(E) Amino acid sequence alignment of the WW tandems from SAV1, KIBRA, and MAGI2 based on the structural alignment shown in (C).

Also see Figure S2 and Table S1.

KIBRA and MAGIs (Ji et al., 2019; Lin et al., 2019). Analytical gel filtration chromatography analysis also showed that mixing of SAV1 WW12ex and dendrin PY23 only induced a very small elution peak shift of dendrin PY23 (Figure 1F), consistent with the very weak interaction between SAV1 WW12ex and dendrin PY23. Sequence alignment analysis of SAV1 WW12ex showed that the extension sequence following the WW domains contains two conserved Pro-rich motifs separated by only two residues: a noncanonical type I WW domain binding PY motif ("VPRY") and a poly-P motif ("PPPψ", where "ψ" is a hydrophobic residue with an aliphatic sidechain; Figure 1A). We postulated that the Pro-rich extension sequence might fold back to bind to the WW12 tandem, forming an autoinhibited structure. Indeed, a weak interaction (K_d ~91 μM) between WW12 and the extension sequence of SAV1 could be detected by ITC (Figure 1G). It is envisaged that the affinity of the binding between WW12 and the extension sequence in *cis* is significantly stronger in SAV1 WW12ex. We further found that SAV1 WW12ex was eluted as a stable and homogeneous dimer on an analytical gel filtration column. Truncating the poly-P motif (i.e., "WW12PY" in Figure 1H) or both the poly-P and PY motifs (i.e., "WW12" in Figure 1H) progressively weakened the dimer formation of SAV1 WW12ex. Collectively, the above biochemical analyses revealed that SAV1 WW12ex forms a stable dimer in solution and the extension sequence is essential for the WW12ex dimer formation.

Crystal Structure of the SAV1 WW12ex Homodimer

To understand the molecular basis governing the SAV1 WW12ex dimerization, we determined the crystal structure of mouse SAV1 WW12ex at the 1.7-Å resolution (Figure 2A; Table S1). Note that mouse and human SAV1 WW12ex differ by only one amino acid residue with Val279 in human replaced by Ile in mouse (Figure 1A). For the convenience of description, we number the residues of SAV1 based on the human sequence, as we will be analyzing numerous SAV1 variants found in patients with cancers. All residues of SAV1 WW12ex (L199–Y281) are well resolved in the electron density map. In the crystal, SAV1 WW12ex adopts a V-shaped homodimer with the Pro-rich extension sequence from one molecule binding to WW12 from another molecule, forming a domain-swapped dimer (Figure 2A). The structure clearly shows that the target binding sites of both WW domains are occupied by the extension sequence, revealing that SAV1 WW12ex indeed adopts an autoinhibited conformation (i.e., the target binding site of the WW tandem is blocked by its own tail extension; Figure 2B). The direct contact between the two WW12 tandems in the WW12ex dimer is minimal, suggesting that the WW2-mediated dimer formation of SAV1 reported earlier (Ohnishi et al., 2007) may not be the main mechanism for the SAV1 dimerization. A structural comparison of the SAV1 WW12 tandem in the WW12ex dimer with the WW12 tandems of KIBRA and MAGI2 in complex with dendrin PY23 revealed that the three WW tandems adopt a similar overall conformation (Figure 2C). Notably, compared to the KBIRA and MAGI2 WW tandems, SAV1 WW12 has a much shorter interdomain linker (12 amino acids [aas] in SAV1 versus 23 or 24 aas in MAGI2 or KIBRA; Figures 2C–2E). The 12-residue linker of SAV1 WW12 (S228–G239) folds into three continuous β-turns to glue the two WW domains into an integral structural unit (Figures 2D and 2E), explaining why the 12-residue linker in vertebrate SAV1 is completely conserved. In KIBRA and MAGI2, the supramodular structures of their WW12 tandems are stabilized by the interactions between the interdomain linker and a C-terminal helix extension (Figures 2C and 2E; also see Lin et al., 2019).

Detailed Interactions between WW12 and the Extension in the SAV1 WW12ex Dimer

In the SAV1 WW12ex dimer, each WW domain forms a canonical β sheet fold with three anti-parallel β strands. Instead of the typical type I WW/PPxY motif interactions, the extension sequence binds to the two WW domains of SAV1 via somewhat unique modes with "PPPI" of the poly-P motif binding to WW1 and "PRY" of the PY motif engaging WW2 (Figures 3A and 3B). Due to the formation of the WW12 supramodule, the distance of two target binding pockets of the WW tandem is fixed and optimal for simultaneously recognizing the PPPI and PRY motifs of the extension separated by only two residues (Ji et al., 2019; Lin et al., 2019). The PPPI motif lies in the hydrophobic groove of WW1. P276 and P277 are sandwiched by two aromatic residues (Y216 from β2 and W227 immediately following β3) in WW1. I279 of the PPPI motif occupies the WW1 hydrophobic pocket that is normally occupied by a Tyr in type I WW domains (Figure 3C). The binding between the PPPI motif and SAV1 WW1 is a type I WW domain/target binding instead of a type II WW/target binding (Figure S2; Meiyappan et al., 2007).

Interestingly, the PRY motif, instead of the canonical four-residue PPxY motif, binds to SAV1 WW2 (Figures 3B and 3C). P271 from the PRY motif nestles in a pocket formed by three aromatic residues from WW2 (F248 from β1′/β2′ loop, Y251 from β2′, and Y262 immediately following β3′). The binding of P271 to SAV1 WW2 is essentially the same as the first Pro in the PPxY motif's binding to the type I WW domain (Figures 3B and 3C). Thus, the backbone of the PRY motif of SAV1 WW12ex adopts a more extended conformation in order to match the length of the backbone of the four-residue PPxY motif bound to a typical type I WW domain (Figure 3C). The sidechain of R272 forms a network of salt bridges with E247 in the β1′/β2′ loop of WW2, D274 in the extension, and R214 from WW1 (Figure 3A). Y273, like the tyrosine residue in the typical PPxY motif, forms a signature hydrogen bond with H255 from the β2′/β3′ loop of WW2 (Figures 3A and 3B).

The structure, together with the amino acid sequence analysis, clearly shows that both WW domains of SAV1 are typical type I WW domains with all key residues necessary for binding to PY motif targets (Figures 3D and 3E). This analysis suggests that, if not autoinhibited, the SAV1 WW12 tandem should be able to bind to two PY-motif repeats arranged right next to each other. Indeed, we detected a robust binding of dendrin PY23 to SAV1 WW12 (K_d ~1.7 μM; Figure 3F). LATS1-PY23 also binds to SAV1 WW12. However, the binding of LATS1-PY23 to SAV1 WW12 is much weaker (K_d ~43 μM) than its binding to WW tandems of KIBRA, MAGI2, and MAGI3 (Figure S3). Additionally, dendrin PY23 binds to WW12PY (i.e., WW12ex with the PPPI motif truncated) and to WW12 with comparable affinities (Figures 3F and 3G), indicating that disrupting the interaction between PPPI motif and WW1 releases the autoinhibition of WW12ex. The above results also imply that the SAV1 WW12 tandem may bind to certain target proteins upon release of its autoinhibition.

Crystal Structure of the SAV1 WW12/Dendrin PY23 Complex

To understand the binding of the SAV1 WW12 tandem to the canonical PPxY motifs, we tried to determine the structure of SAV1 WW12 in complex with dendrin PY23. Mixing SAV1 WW12 and dendrin PY23 at a 1:1 ratio resulted in a homogeneous and monomeric complex peak (Figure S4A). The structural determination of the SAV1 WW12/dendrin PY23 complex (Figure 4A; Table S1) was facilitated by fusing dendrin PY23 to the C terminus of SAV1 WW12. The fusion protein was shown as a homogeneous dimer on an analytical gel filtration column (Figure S4B). The structures of the SAV1 WW tandem in the WW12ex dimer and in the dendrin PY23-bound complex are extremely similar with (root-mean-square deviation [RMSD] value of their backbones of ~0.7 Å; Figure 4B). The structure of the complex confirms that both WW domains can bind to the type I WW targets containing PPxY motifs (Figure 4A).

Careful inspection of the interaction between the dendrin PPPY motif and SAV1 WW2 showed that the first Pro in the motif is not involved in the binding (Figures 4A and 4C). Interestingly, changing the PPPY motif of dendrin into "PPDY" weakened the dendrin PY23/SAV1 WW12 binding by ~18 fold, but changing the PPPY motif into "DPPY" did not decrease the binding at all. Replacing the Pro preceding Tyr in the PPPY motif with Arg also weakened

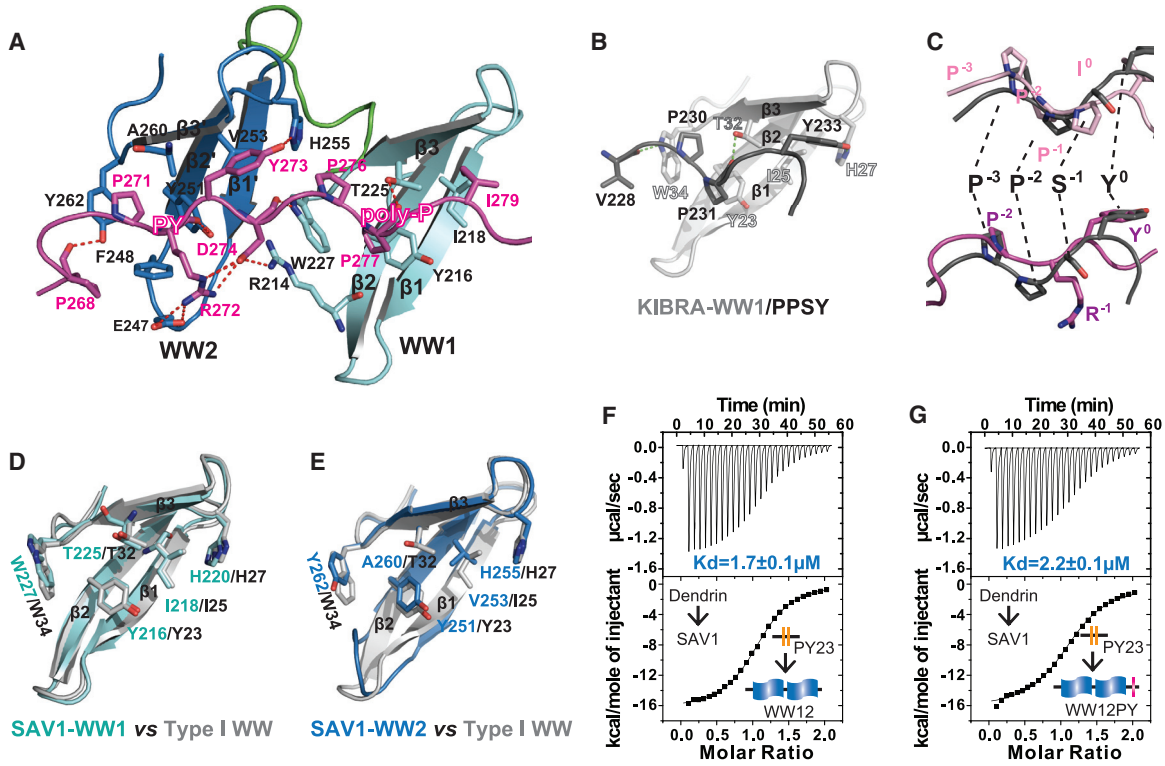

Figure 3. Detailed Interactions between WW12 and the Extension of SAV1

(A) Combined ribbon and stick model showing the detailed interactions between WW12 and the extension in the SAV1 WW12ex dimer.

(B) Ribbon-stick model showing detailed interactions of the classical type I WW/PPxY motif binding observed in the KIBRA WW tandem in complex with dendrin PY23.

(C) Comparisons of the conformation of the "PPPI" (top) and "PRY" (bottom) sequences observed in the SAV1 WW12ex structure with the conformation of a classical "PPSY" sequence bound to a type I WW domain.

(D and E) Ribbon-stick model showing that WW1 (D) and WW2 (E) of SAV1 are typical type I WW domains containing all key residues required for binding to PY motif targets.

(F and G) ITC-based measurements showing that WW12 (F) and WW12PY (G) of SAV1 can robustly bind to dendrin PY23 due to truncation-induced releases of the autoinhibition of SAV1 WW12ex.

Also see Figures S2 and S3.

the binding by ~9 fold. Therefore, SAV1 WW2 can only recognize a 3-residue motif (i.e., PRY motif in Figure 3A and PPY motif in Figure 4A) with the optimal sequence of "PPY". It is noted that the second last residue of β3 in most of the type I WW domain is a Thr, and the side chain of this Thr forms a strong hydrogen bond with the backbone of the Pro^{-2} in the PPxY motif (i.e., "P^{-3}P^{-2}xY^{0}"), thus stabilizing the turn-like structure of the "PxY" sequence (Figures 4A and 4C). In SAV1 WW2, the second last residue of β3′ is an Ala, which cannot form any hydrogen bond with Pro^{-2}. The two Pro residues in the PPY motif assume the same binding mode as the two Pro residues in the canonical PPxY-motif containing ligands (Figures 4A and 4C). Taken together, the above structural and biochemical analyses indicate that the optimal target binding sequence for the SAV1 WW12 tandem is "PPYxxPPxY," where x can be various amino acid residues.

Phosphomimetic Y273E Mutation Can Release the Autoinhibition of SAV1 WW12ex

In SAV1 WW12ex dimer, Y273 is critical for the PRY motif to bind to WW2 (Figure 5A). It is envisaged that potential phosphorylation of Y273 in the PRY motif may release the autoinhibition of SAV1 WW12ex. Phosphorylation of the Tyr residue in the "PPPY" motif of β-dystroglycan has been reported (James et al., 2000; Ilsley et al., 2001), and the PPPY motif of β-dystroglycan is required for its tight binding to the KIBRA WW tandem (Lin et al., 2019). We substituted Y273 with glutamic acid to mimic its phosphorylation. Strikingly, compared with the wild-type protein, the Y273E mutant of SAV1 WW12ex failed to form a stable dimer (Figure 5B). Concomitantly, dendrin PY23 was able to bind to Y273E-WW12ex with a much stronger affinity than to the wild-type (WT) WW12ex (K_d ~3.8 μM versus ~39 μM; Figure 5C versus Figure S1A). The above biochemical data suggest that phosphorylation of Y273 can release the autoinhibition of the SAV1 WW12ex. It will be important to investigate in the future whether phosphorylation of Y273 may indeed occur for SAV1 *in vivo*.

WW12ex-Mediated SAV1 Dimerization Is Essential for MST/SAV1 Complex Assembly upon Hippo Activation

In solution, SAV1 WW12ex formed a stable dimer, and its elution volume did not change when the concentrations of protein were

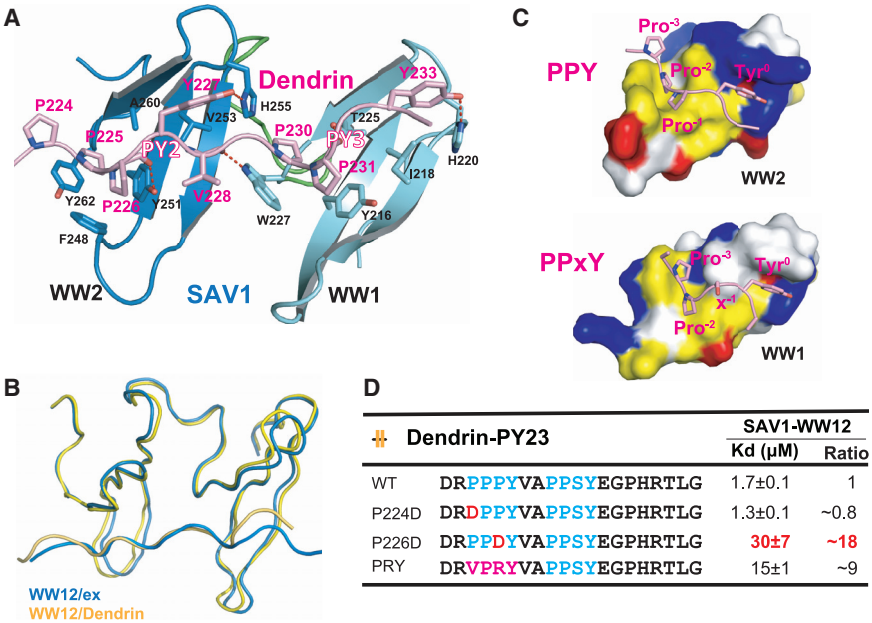

D

Dendrin-PY23		SAV1-WW12 Kd (μM)	SAV1-WW12 Ratio
WT	DRPPPYVAPPSYEGPHRTLG	1.7±0.1	1
P224D	DRDPPYVAPPSYEGPHRTLG	1.3±0.1	~0.8
P226D	DRPPDYVAPPSYEGPHRTLG	30±7	~18
PRY	DRVPRYVAPPSYEGPHRTLG	15±1	~9

Figure 4. Crystal Structure of the SAV1 WW12/Dendrin PY23 Complex

(A) Combined ribbon and stick diagram showing the structure and detailed interaction of SAV1 WW12 in complex with dendrin PY23.

(B) Superimposition of the structures of the SAV1 WW tandems from the WW12ex dimer and from the complex between SAV1 WW12 and dendrin PY23.

(C) Combined surface and ribbon-stick diagram showing the binding of SAV1 WW2 with the "PPPY" motif of dendrin and the binding of SAV1 WW1 with the PPSY motif of dendrin.

(D) ITC-based measurements quantifying the binding of SAV1 WW12 to WT and various mutants of dendrin PY23.

Also see Figure S4 and Table S1.

varied (Figure 5D). However, the various WW12ex truncation mutants (Figure 1H) or the Y273E mutant (Figure 5B) were eluted at volumes between a dimer and a monomer on the gel filtration column. Additionally, when the concentration of the Y273E-WW12ex increased, its elution volume became smaller (Figure 5D). The above analysis indicated that the WW12ex truncation mutants or the Y273E-WW12ex mutant formed weak dimers in solution. We speculated that such weak dimerization of the WW12ex variants is mediated by WW2, as WW2 was reported to form homodimer in solution (Ohnishi et al., 2007). In the NMR structure of the WW2 dimer, Ser245 is in the dimeric interface (Figure 5E), and substitution of S245 with Asp converted WW12 into a homogeneous monomer (Figure S5A). Replacing S245 with Asp also converted Y273E-WW12ex into a homogeneous monomer. In contrast, if only S245 was replaced by Asp, this SAV1 WW12ex mutant remained as a stable dimer in solution (Figures 5B and S5A). Thus, the dimerization of SAV1 WW12ex is determined by the tail extension sequence instead of the previous reported WW2 (Figure 5F).

We next used SAV1 knockout (KO) HEK293A cells that were characterized previously (Plouffe et al., 2016) to test the dimerization property of the full-length SAV1. The FLAG-tagged WT SAV1 could pull down the Myc-tagged SAV1 expressed in SAV1 KO HEK293A cells (Figure 5G). Neither the FLAG-tagged SAV1-Y273E nor the SAV1-Y273E/S245D bound to the Myc-tagged WT SAV1. In contrast, the FLAG-tagged SAV1-S245D could still bind to the Myc-tagged WT SAV1, suggesting that the previously reported WW2-mediated SAV1 dimerization might be an *in vitro* experimental artifact.

We further generated stable cell pools by re-expressing WT SAV1 or various SAV1 mutants in SAV1 KO cells to test the MST/SAV1 complex formation upon Hippo pathway stimulation by serum deprivation (Miller et al., 2012; Yu et al., 2012). Under the Hippo off state (+fetal bovine serum [FBS]), WT and each mutant SAV1 bound to MST1 at a similar level using a co-immunoprecipitation-based assay (Figure 5H), indicating that the WW12ex-mediated SAV1 dimerization does not play a critical role in the interaction between SAV1 and MST1 under the Hippo off status. However, upon Hippo activation by serum starvation (−FBS), SAV1 KO HEK293A cells expressing SAV1-Y273E or SAV1-Y273E/S245D showed diminished MST1 and SAV1 complex formation when compared to the cells expressing WT or S245D SAV1 (Figure 5H). The above data support that WW12ex-mediated SAV1 dimerization is important for the MST and SAV1 complex assembly during the Hippo signal on state. Moreover, cells expressing SAV1-Y273E/S245D or SAV-Y273E (to a less extent) showed diminished LATS1 phosphorylation under serum starvation (Figure S5B), further indicating that the WW12ex-mediated SAV1 dimer formation is important for MST activation and subsequent LATS phosphorylation.

SAV1 Variants within WW12ex Found in Patients with Cancers Are Defective in Dimer Formation

We searched the COSMIC database (https://cancer.sanger.ac.uk/cosmic) and identified eight SAV1 variants distributed throughout the WW12ex region of the protein from patients with cancers (Figures 6A and 6B). Except for the R214K and S245L, the rest of the six variants were found to impair either SAV1 WW12ex dimer formation and/or target binding (assayed using dendrin PY23 as a putative target for the binding assay; Figures 6C, 6D, and S6). Analytical gel filtration chromatography analysis clearly showed that the R233Q, D254H, Y262H, and Y273H mutations of SAV1 WW12ex all displayed impaired dimer formation (Figures 6C and 6D; cf. the Y273E-WW12ex mutant in Figure 5). R233 is in the second β-turn in the completely conserved WW12 linker; it forms a network of hydrogen bonds with the residues from both WW domains (W227, S228, and H229 in WW1 and E241 in WW2; Figure 6B1) to stabilize the two WW domains into a structural supramodule (Figure 2). Therefore, R233Q mutation is expected to disturb the structural coupling of the WW12 tandem and consequently impair the

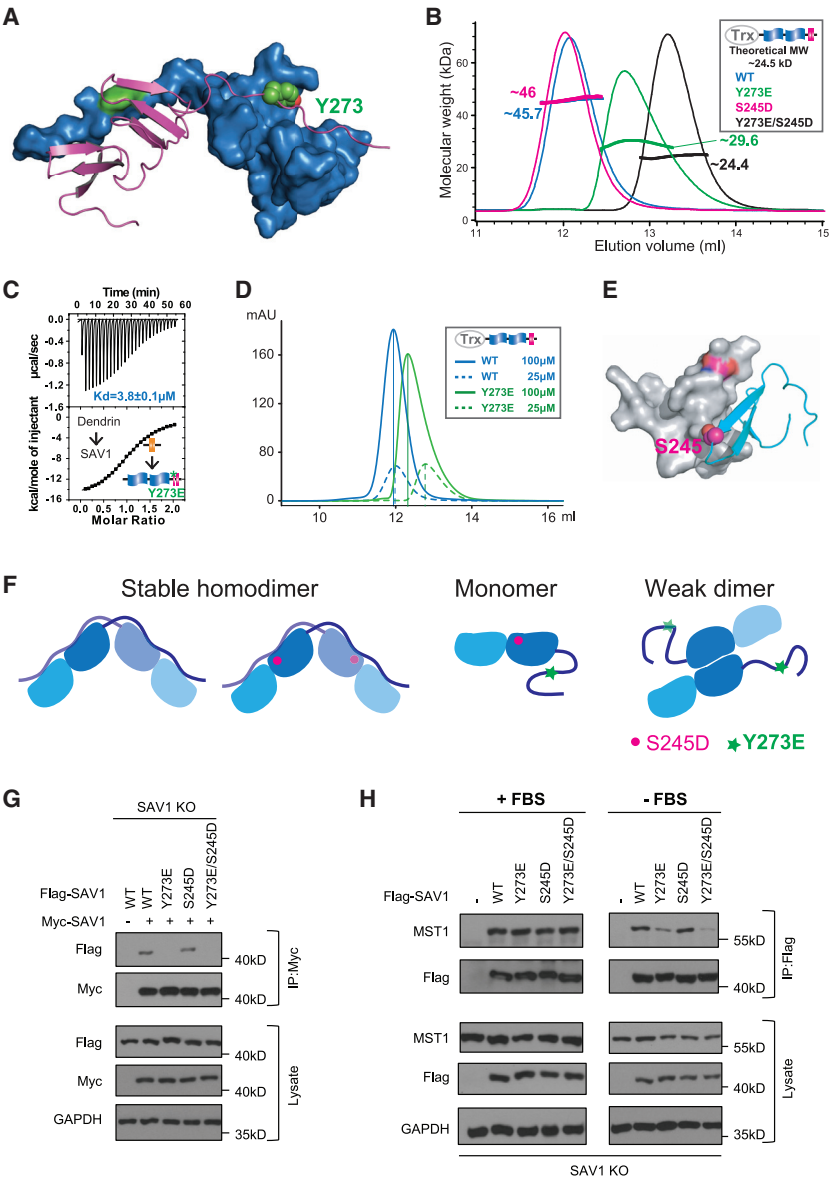

Figure 5. WW12ex-Mediated SAV1 Dimerization Is Essential for the MST/SAV1 Complex Assembly upon Hippo Activation

(A) Combined surface and ribbon-stick model showing that Y273 is critical for the SAV1 WW12ex dimer structure formation.

(B) Analytical gel filtration chromatography coupled with static light scattering analysis showing the dimeric state of SAV1 WW12ex WT and its various mutants.

(C) ITC-based measurement showing that SAV1 Y273E-WW2ex can robustly bind to dendrin PY23, suggesting that phosphorylation of Y273 releases the autoinhibited conformation of SAV1 WW12ex.

(D) Analytical gel filtration chromatography showing that SAV1 WW12ex, but not Y273E-WW12ex mutant, forms a stable dimer in solution.

(E) Combined surface and ribbon-stick model showing that S245 is located in the dimer interface of the isolated SAV1 WW2 dimer structure (PDB: 2DWV) derived from NMR-based study.

(F) Cartoon model showing the dimer formation of WT SAV1 WW12ex and the impact of various mutants on the dimer assembly.

(G) Co-immunoprecipitation-based assay showing the self-association of WT and various SAV1 mutants expressed in SAV1 KO HEK293A cells.

(H) Co-immunoprecipitation-based assay showing the effect of SAV1 mutations on the MST/SAV1 complex formation at the Hippo pathway off ("+FBS") and on ("−FBS") conditions.

Also see Figure S5.

SAV1 WW12ex dimer formation and its putative target binding (Figure S6B). The R233Q mutation has been reported to impair the tumor-suppression ability of SAV1 in mice (Jiang et al., 2019). D254 is at the end of β2′ of WW2; it forms several hydrogen bonds with the backbones of T256 and N257 in the β2′/β3′ loop, thus stabilizing the loop conformation (Figure 6B2). H255 in the β2′/β3′ loop is a signature residue in the type I WW domain, as it recognizes Tyr in the PPxY motif of targets, including the PRY motif in the extension sequence of SAV1. Y262 is at the end of β3′ of WW2; its aromatic ring stacks with the Pro residue from the PRY motif of the extension sequence (Figure 6B3) or the Pro^{-2} residue from the PPPY motif of dendrin PY23 (Figure 4A). Thus, the D254H mutation or the Y262H mutation weakens the SAV1 dimer formation and its putative target binding (Figures 6C, 6D, and S6B). The Y273H mutant of SAV1 WW12ex should behave very much like the Y273E mutant as detailed in Figure 5. The R214K or the S245L mutation had minimal impact on the dimer formation or the putative target binding of SAV1 WW12 (Figure S6).

W209 forms hydrophobic interactions with V207 and K215 in the folding core of WW1 (Figure 6B4). Although W209 is not directly involved in the WW12ex supramodule formation or autoinhibition, the W209C mutation may destabilize the overall folding of WW12ex and thus can weaken its dimer formation and putative target binding (Figure S6). T224, analogous to D254 in WW2, stabilizes backbone conformation of the β2/β3 loop, thus facilitating H220 in the loop to binding to the Tyr residue in the PPxY motif (Figure 6B4). Accordingly, the T224H mutant of SAV1 WW12 displayed a significantly reduced binding to dendrin PY23 (Figure S6B).

DISCUSSION

The detailed structural and biochemical analysis presented in this study demonstrated that SAV1 uses its WW12 tandem and an extension sequence immediately following the tandem to form a stable, domain-swapped dimer (Figure 2). The extension sequence contains two sub-optimal type I WW-binding motifs that directly bind to both WW domains, thus assembling SAV1 into a dimer and concomitantly keeping its WW tandem from binding to potential proteins (Figure 3). It should be noted that

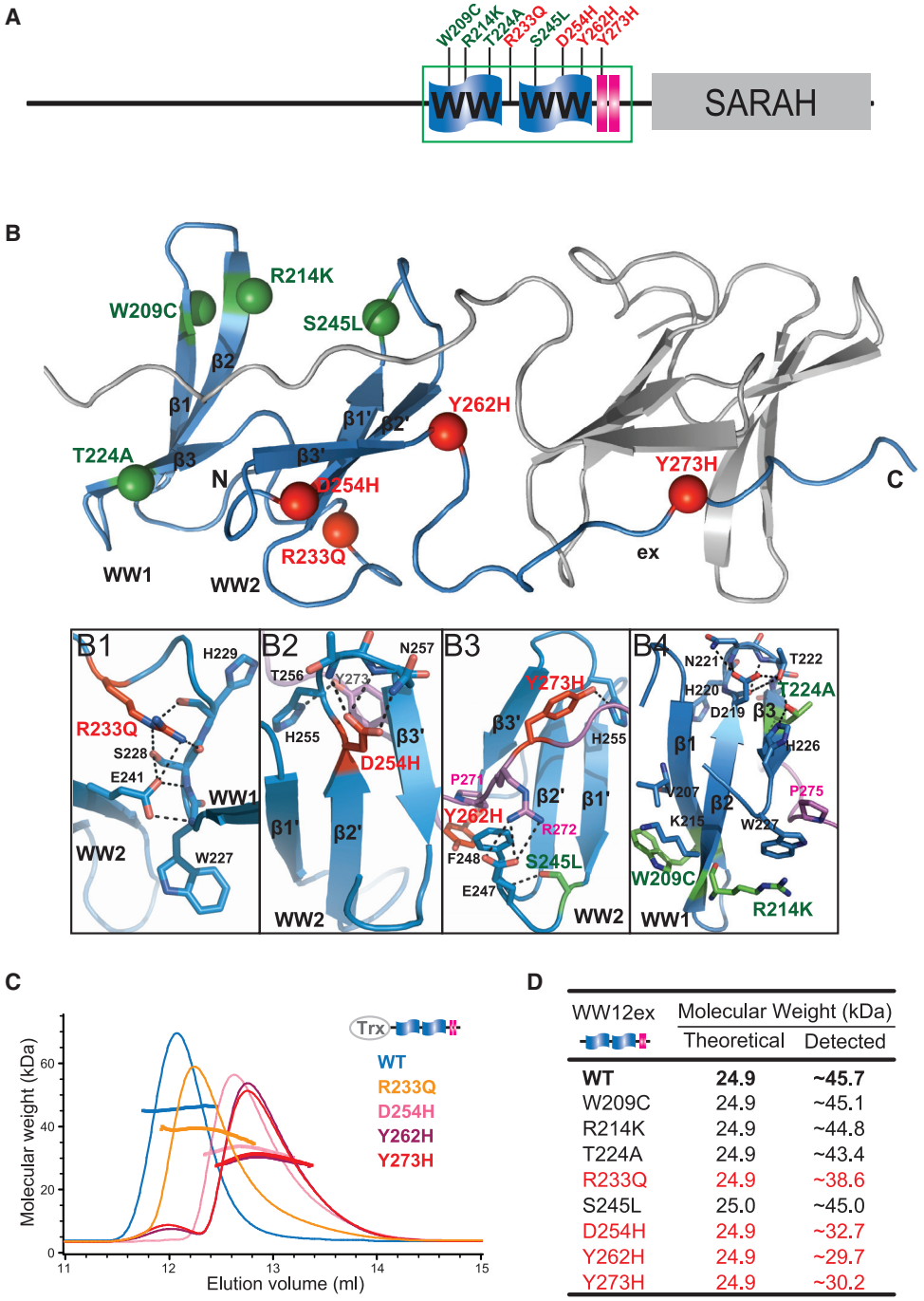

D

WW12ex	Molecular Weight (kDa)	
	Theoretical	Detected
WT	**24.9**	**~45.7**
W209C	24.9	~45.1
R214K	24.9	~44.8
T224A	24.9	~43.4
R233Q	24.9	~38.6
S245L	25.0	~45.0
D254H	24.9	~32.7
Y262H	24.9	~29.7
Y273H	24.9	~30.2

Figure 6. Impact of SAV1 Variants Found in Patients with Cancers on the SAV1 WW12ex Dimer Formation

(A and B) Schematic diagram (A) and ribbon-dot model (B) summarizing eight SAV1 variants in the WW12ex region found in patients with cancers. The mutations that obviously impair the dimer formation of SAV1 are colored in red. The panels in B1–B4 show the detailed structural roles of the residues found in the variants.

(C) Analytical gel filtration chromatography coupled with static light scattering analyses of SAV1 WW12ex and its variants with impaired dimer formation.

(D) Summary of molecular weights of the analyzed SAV1 WW12ex mutants derived from the analytical gel filtration chromatography coupled with static light scattering analyses.

Also see Figure S6.

the autoinhibited conformation of SAV1 WW12ex referred here is specifically defined as potential target binding of the WW tandem. The formation of the WW12ex homodimer does not inhibit the function of SAV1. Instead, the WW12ex homodimer formation is important for SAV1 to form complex with MST and thus critical for SAV1's function. Our structural analysis revealed that Y273 in the extension sequence is critical for forming the SAV1 WW12ex homodimer. Replacing Y273 with Glu dramatically weakens the SAV1 WW12ex dimer formation and the interaction between SAV1 and MST when the Hippo signaling is on (Figure 5). It is tempting to speculate that phosphorylation of Y273 may function as a regulatory switch in modulating SAV1's activity in the Hippo core kinase signaling cascade.

Analogous to the WW tandems from KIBRA and MAGIs (Ji et al., 2019; Lin et al., 2019), the direct conformational coupling between the two WW domains in the SAV1 WW12 tandem is critical for its autoinhibition and putative target binding. By direct conformational coupling, the distance between the target binding pockets of the two WW domains in each of these WW tandems is fixed and optimal for binding to two consecutive PY-motif-containing peptides in target proteins. Consequently, these WW tandems can bind to target proteins with very high affinities. Given that most of WW domain proteins contain multiple WW domains arranged in tandem, these tandemly arranged WW domains may also function as supramodules.

Previous studies showed that SAV1 recruits MST1/2 through their SARAH domains (Pantalacci et al., 2003; Callus et al., 2006; Bae et al., 2017; Cairns et al., 2018). In this study, we found that, when the Hippo signal is off, the interaction between SAV1 and MST does not depend on SAV1-WW12ex-mediated dimerization. However, when the Hippo signal is on, the assembly of the MST/SAV1 complex and the kinase activity of MST require SAV1 WW12ex homodimerization (Figures 5G, 5H, and S4B). It is possible that the WW12ex-mediated SAV1 dimer formation may facilitate incorporation of additional components, such as STRIPAK or Merlin/NF2, to the MST/SAV1 assembly upon the activation of the Hippo pathway (Yu et al., 2010; Bae et al., 2017). Further experiments will be needed to test the above possibility.

Finally, our structural and biochemical analysis of the eight SAV1 variants found in patients with cancers revealed that a number of such variants impair SAV1 dimer formation and subsequent MST activation (Figures 5G, 5H, and 6). Therefore, these variants can be deleterious by impairing the tumor-suppressing activity of SAV1. The SAV1 WW12ex structure will be useful to analyze additional variants within SAV1 WW12ex that may be identified in the future.

STAR★METHODS

Detailed methods are provided in the online version of this paper and include the following:

- KEY RESOURCES TABLE
- RESOURCE AVAILABILITY
  - Lead Contact
  - Materials Availability
  - Data and Code Availability
- EXPERIMENTAL MODEL AND SUBJECT DETAILS
  - Cell lines
- METHOD DETAILS
  - Constructs, Protein Expression and Purification
  - Crystallization and Data Collection
  - Structure Determination and Refinement
  - Isothermal Titration Calorimetry Assay
  - Analytical Gel Filtration Chromatography Coupled with Static Light Scattering
  - Transfection and Lentiviral Infection
  - Immunoblotting and Immunoprecipitation
- QUANTIFICATION AND STATISTICAL ANALYSIS

SUPPLEMENTAL INFORMATION

Supplemental Information can be found online at https://doi.org/10.1016/j.celrep.2020.108118.

ACKNOWLEDGMENTS

We thank the BL19U1 beamline at National Facility for Protein Science Shanghai (NFPS) and BL17U1 beamline at Shanghai Synchrotron Radiation Facility (SSRF) for X-ray beam time. This work was supported by grants from RGC of Hong Kong (AoE-M09-12 and C6004-17G), a grant from Asia Foundation for Cancer Research (AFCR17SC01) to M.Z., and grants from National Institutes of Health (CA196878, CA217642, GM51586, and DEO15964) to K.G. M.Z. is a Kerry Holdings Professor in Science, a Senior Scholar of the Croucher Foundation, and a Senior Fellow of IAS at HKUST.

AUTHOR CONTRIBUTIONS

Z.L. and R.X. performed experiments; Z.L., R.X., K.G., and M.Z. designed the research and analyzed data; Z.L. and M.Z. drafted and all authors commented on the manuscript; and M.Z. coordinated the project.

DECLARATION OF INTERESTS

K.G. is a co-founder and has an equity interest in Vivace Therapeutics. The terms of this arrangement have been reviewed and approved by the University of California, San Diego in accordance with its conflict-of-interest policies.

Received: March 29, 2020
Revised: June 27, 2020
Accepted: August 17, 2020
Published: September 8, 2020

REFERENCES

Adams, P.D., Afonine, P.V., Bunkóczi, G., Chen, V.B., Davis, I.W., Echols, N., Headd, J.J., Hung, L.W., Kapral, G.J., Grosse-Kunstleve, R.W., et al. (2010). PHENIX: a comprehensive Python-based system for macromolecular structure solution. Acta Crystallogr. D Biol. Crystallogr. *66*, 213–221.

Bae, S.J., Ni, L., Osinski, A., Tomchick, D.R., Brautigam, C.A., and Luo, X. (2017). SAV1 promotes Hippo kinase activation through antagonizing the PP2A phosphatase STRIPAK. eLife *6*, e30278.

Cairns, L., Tran, T., Fowl, B.H., Patterson, A., Kim, Y.J., Bothner, B., and Kavran, J.M. (2018). Salvador has an extended SARAH domain that mediates binding to Hippo kinase. J. Biol. Chem. *293*, 5532–5543.

Callus, B.A., Verhagen, A.M., and Vaux, D.L. (2006). Association of mammalian sterile twenty kinases, Mst1 and Mst2, with hSalvador via C-terminal coiled-coil domains, leads to its stabilization and phosphorylation. FEBS J. *273*, 4264–4276.

Chong, P.A., Lin, H., Wrana, J.L., and Forman-Kay, J.D. (2010). Coupling of tandem Smad ubiquitination regulatory factor (Smurf) WW domains modulates target specificity. Proc. Natl. Acad. Sci. USA *107*, 18404–18409.

Emsley, P., Lohkamp, B., Scott, W.G., and Cowtan, K. (2010). Features and development of Coot. Acta Crystallogr. D Biol. Crystallogr. *66*, 486–501.

Fulford, A., Tapon, N., and Ribeiro, P.S. (2018). Upstairs, downstairs: spatial regulation of Hippo signalling. Curr. Opin. Cell Biol. *51*, 22–32.

Hauri, S., Wepf, A., van Drogen, A., Varjosalo, M., Tapon, N., Aebersold, R., and Gstaiger, M. (2013). Interaction proteome of human Hippo signaling: modular control of the co-activator YAP1. Mol. Syst. Biol. *9*, 713.

Ilsley, J.L., Sudol, M., and Winder, S.J. (2001). The interaction of dystrophin with beta-dystroglycan is regulated by tyrosine phosphorylation. Cell. Signal. *13*, 625–632.

James, M., Nuttall, A., Ilsley, J.L., Ottersbach, K., Tinsley, J.M., Sudol, M., and Winder, S.J. (2000). Adhesion-dependent tyrosine phosphorylation of (beta)-dystroglycan regulates its interaction with utrophin. J. Cell Sci. *113*, 1717–1726.

Ji, Z., Li, H., Yang, Z., Huang, X., Ke, X., Ma, S., Lin, Z., Lu, Y., and Zhang, M. (2019). Kibra modulates learning and memory via binding to dendrin. Cell Rep. *26*, 2064–2077.e7.

Jiang, J., Chang, W., Fu, Y., Gao, Y., Zhao, C., Zhang, X., and Zhang, S. (2017). SAV1 represses the development of human colorectal cancer by regulating the Akt-mTOR pathway in a YAP-dependent manner. Cell Prolif. *50*, e12351.

Jiang, Y., Zhang, Y., Leung, J.Y., Fan, C., Popov, K.I., Su, S., Qian, J., Wang, X., Holtzhausen, A., Ubil, E., et al. (2019). MERTK mediated novel site Akt phosphorylation alleviates SAV1 suppression. Nat. Commun. *10*, 1515.

Kwon, Y., Vinayagam, A., Sun, X., Dephoure, N., Gygi, S.P., Hong, P., and Perrimon, N. (2013). The Hippo signaling pathway interactome. Science *342*, 737–740.

Lin, Z., Yang, Z., Xie, R., Ji, Z., Guan, K., and Zhang, M. (2019). Decoding WW domain tandem-mediated target recognitions in tissue growth and cell polarity. eLife *8*, e49439.

Ma, S., Meng, Z., Chen, R., and Guan, K.L. (2019). The Hippo pathway: biology and pathophysiology. Annu. Rev. Biochem. *88*, 577–604.

Mana-Capelli, S., and McCollum, D. (2018). Angiomotins stimulate LATS kinase autophosphorylation and act as scaffolds that promote Hippo signaling. J. Biol. Chem. *293*, 18230–18241.

Matsuura, K., Nakada, C., Mashio, M., Narimatsu, T., Yoshimoto, T., Tanigawa, M., Tsukamoto, Y., Hijiya, N., Takeuchi, I., Nomura, T., et al. (2011). Downregulation of SAV1 plays a role in pathogenesis of high-grade clear cell renal cell carcinoma. BMC Cancer *11*, 523.

McCoy, A.J., Grosse-Kunstleve, R.W., Adams, P.D., Winn, M.D., Storoni, L.C., and Read, R.J. (2007). Phaser crystallographic software. J. Appl. Cryst. *40*, 658–674.

Mehra, R., Vats, P., Cieslik, M., Cao, X., Su, F., Shukla, S., Udager, A.M., Wang, R., Pan, J., Kasaian, K., et al. (2016). Biallelic alteration and dysregulation of the Hippo pathway in mucinous tubular and spindle cell carcinoma of the kidney. Cancer Discov. *6*, 1258–1266.

Meiyappan, M., Birrane, G., and Ladias, J.A.A. (2007). Structural basis for polyproline recognition by the FE65 WW domain. J. Mol. Biol. *372*, 970–980.

Miller, E., Yang, J., DeRan, M., Wu, C., Su, A.I., Bonamy, G.M., Liu, J., Peters, E.C., and Wu, X. (2012). Identification of serum-derived sphingosine-1-phosphate as a small molecule regulator of YAP. Chem. Biol. *19*, 955–962.

Min, B., Kim, M.K., Zhang, J.W., Kim, J., Chung, K.C., Oh, B.C., Stein, G.S., Lee, Y.H., van Wijnen, A.J., and Bae, S.C. (2012). Identification of RUNX3 as a component of the MST/Hpo signaling pathway. J. Cell. Physiol. *227*, 839–849.

Minor, W., Cymborowski, M., Otwinowski, Z., and Chruszcz, M. (2006). HKL-3000: the integration of data reduction and structure solution–from diffraction images to an initial model in minutes. Acta Crystallogr. D Biol. Crystallogr. *62*, 859–866.

Moya, I.M., and Halder, G. (2019). Hippo-YAP/TAZ signalling in organ regeneration and regenerative medicine. Nat. Rev. Mol. Cell Biol. *20*, 211–226.

Ni, L., Zheng, Y., Hara, M., Pan, D., and Luo, X. (2015). Structural basis for Mob1-dependent activation of the core Mst-Lats kinase cascade in Hippo signaling. Genes Dev. *29*, 1416–1431.

Ohnishi, S., Güntert, P., Koshiba, S., Tomizawa, T., Akasaka, R., Tochio, N., Sato, M., Inoue, M., Harada, T., Watanabe, S., et al. (2007). Solution structure of an atypical WW domain in a novel beta-clam-like dimeric form. FEBS Lett. *581*, 462–468.

Otwinowski, Z., and Minor, W. (1997). Processing of X-ray diffraction data collected in oscillation mode. Methods Enzymol. *276*, 307–326.

Pan, D. (2010). The hippo signaling pathway in development and cancer. Dev. Cell *19*, 491–505.

Pantalacci, S., Tapon, N., and Léopold, P. (2003). The Salvador partner Hippo promotes apoptosis and cell-cycle exit in Drosophila. Nat. Cell Biol. *5*, 921–927.

Plouffe, S.W., Meng, Z., Lin, K.C., Lin, B., Hong, A.W., Chun, J.V., and Guan, K.L. (2016). Characterization of Hippo pathway components by gene inactivation. Mol. Cell *64*, 993–1008.

Salah, Z., Alian, A., and Aqeilan, R.I. (2012). WW domain-containing proteins: retrospectives and the future. Front. Biosci. *17*, 331–348.

Sohn, B.H., Shim, J.J., Kim, S.B., Jang, K.Y., Kim, S.M., Kim, J.H., Hwang, J.E., Jang, H.J., Lee, H.S., Kim, S.C., et al. (2016). Inactivation of Hippo pathway is significantly associated with poor prognosis in hepatocellular carcinoma. Clin. Cancer Res. *22*, 1256–1264.

Sudol, M., and Hunter, T. (2000). NeW wrinkles for an old domain. Cell *103*, 1001–1004.

Sun, S., and Irvine, K.D. (2016). Cellular organization and cytoskeletal regulation of the Hippo signaling network. Trends Cell Biol. *26*, 694–704.

Tapon, N., Harvey, K.F., Bell, D.W., Wahrer, D.C., Schiripo, T.A., Haber, D., and Hariharan, I.K. (2002). salvador Promotes both cell cycle exit and apoptosis in Drosophila and is mutated in human cancer cell lines. Cell *110*, 467–478.

Vargas, R.E., Duong, V.T., Han, H., Ta, A.P., Chen, Y., Zhao, S., Yang, B., Seo, G., Chuc, K., Oh, S., et al. (2020). Elucidation of WW domain ligand binding specificities in the Hippo pathway reveals STXBP4 as YAP inhibitor. EMBO J. *39*, e102406.

Wang, W., Li, X., Huang, J., Feng, L., Dolinta, K.G., and Chen, J. (2014). Defining the protein-protein interaction network of the human hippo pathway. Mol. Cell. Proteomics *13*, 119–131.

Wang, L., Wang, Y., Li, P.P., Wang, R., Zhu, Y., Zheng, F., Li, L., Cui, J.J., and Wang, L.W. (2016). Expression profile and prognostic value of SAV1 in patients with pancreatic ductal adenocarcinoma. Tumour Biol. Published online October 17, 2016. https://doi.org/10.1007/s13277-016-5457-4.

Williams, C.J., Headd, J.J., Moriarty, N.W., Prisant, M.G., Videau, L.L., Deis, L.N., Verma, V., Keedy, D.A., Hintze, B.J., Chen, V.B., et al. (2018). MolProbity: more and better reference data for improved all-atom structure validation. Protein Sci. *27*, 293–315.

Won, G.W., Sung, M., Lee, Y., and Lee, Y.H. (2019). MST2 kinase regulates osteoblast differentiation by phosphorylating and inhibiting Runx2 in C2C12 cells. Biochem. Biophys. Res. Commun. *512*, 591–597.

Yu, J., Zheng, Y., Dong, J., Klusza, S., Deng, W.M., and Pan, D. (2010). Kibra functions as a tumor suppressor protein that regulates Hippo signaling in conjunction with Merlin and Expanded. Dev. Cell *18*, 288–299.

Yu, F.X., Zhao, B., Panupinthu, N., Jewell, J.L., Lian, I., Wang, L.H., Zhao, J., Yuan, H., Tumaneng, K., Li, H., et al. (2012). Regulation of the Hippo-YAP pathway by G-protein-coupled receptor signaling. Cell *150*, 780–791.

Yu, F.X., Zhao, B., and Guan, K.L. (2015). Hippo pathway in organ size control, tissue homeostasis, and cancer. Cell *163*, 811–828.

Zheng, Y., and Pan, D. (2019). The Hippo signaling pathway in development and disease. Dev. Cell *50*, 264–282.

STAR★METHODS

KEY RESOURCES TABLE

REAGENT or RESOURCE	SOURCE	IDENTIFIER
Antibodies		
Rabbit monoclonal anti-LATS1	Cell Signaling Technology	Cat#3477; RRID: AB_2133513
Rabbit monoclonal anti-pLATS1	Cell Signaling Technology	Cat#8654S; RRID: AB_10971635
Rabbit polyclonal anti-MST1	Cell Signaling Technology	Cat#3682; RRID: AB_2144632
Rabbit monoclonal anti-SAV1	Cell Signaling Technology	Cat#13301; RRID: AB_2798176
Rabbit monoclonal anti-Myc	Cell Signaling Technology	Cat#2278; RRID: AB_490778
Rabbit polyclonal anti-c-myc	Santa Cruz	Cat#sc-789; RRID: AB_631274
Rabbit polyclonal anti-GAPDH	Santa Cruz	Cat#sc-25778; RRID: AB_10167668
Mouse monoclonal anti-Flag	Sigma-Aldrich	Cat#F1804; RRID: AB_262044
Bacterial and Virus Strains		
Escherichia coli: BL21(DE3)	Novagen	Cat #69450
Chemicals, Peptides, and Recombinant Proteins		
Recombinant protein: SAV1 WW12ex (aa E198-Q285, Trx tag	Lin et al., 2019	UniProt: Q8VEB2
Recombinant protein: SAV1 WW12PY (aa E198-Q276), Trx tag	This paper	UniProt: Q8VEB2
Recombinant protein: SAV1 WW12 (aa E198-A268), Trx tag	This paper	UniProt: Q8VEB2
Recombinant protein: SAV1 ex (aa A268-Q285)	This paper	UniProt: Q8VEB2
Recombinant protein: Dendrin PY23 (aa D222-G241), Trx tag	This paper	UniProt: Q80TS7
Recombinant protein: LATS1 PY1-4 (aa N361-E582), Trx tag	Lin et al., 2019	UniProt: Q8BYR2
Recombinant protein: LATS1 PY23 (aa V545-S568), Trx tag	Lin et al., 2019	UniProt: Q8BYR2
Recombinant protein: PTPN14 PY12 (aa A433-G455), Trx tag	Lin et al., 2019	UniProt: Q15678
Recombinant protein: AMOTL1 PY34 (aa R307-T327), Trx tag	This paper	UniProt: Q8IY63
Recombinant protein: SAV1 WW12 (aa E198-V271) fused Dendrin PY23 (aa P224-G235)	This paper	UniProt: Q8VEB2/ Q80TS7
PolyJet	SignaGen Laboratories	Cat#SL100688
Pierce Protein A/G Magnetic Beads	Thermo Fisher Scientific	Cat#88803
cOmplete, EDTA-free Protease Inhibitor Cocktail	Roche	Cat#11873580001
Deposited Data		
SAV1 WW12ex structure	This paper	PDB: 7BQF
SAV1 WW12 and Dendrin PY23 complex structure	This paper	PDB: 7BQG
Experimental Models: Cell Lines		
Human: HEK293A	Plouffe et al., 2016	N/A
Human: HEK293A SAV1 dKO	Plouffe et al., 2016	N/A
Human: HEK293A SAV1 dKO Flag-SAV1	This paper	N/A
Human: HEK293A SAV1 dKO Flag-SAV1-Y273E	This paper	N/A

(*Continued on next page*)

Continued

REAGENT or RESOURCE	SOURCE	IDENTIFIER
Human: HEK293A SAV1 dKO Flag-SAV1-S245D	This paper	N/A
Human: HEK293A SAV1 dKO Flag-SAV1 Y273E/S245D	This paper	N/A
Recombinant DNA		
Plasmid: Myc-SAV1 full length	This paper	NCBI: NM_021818
Software and Algorithms		
HKL2000	HKL Research Inc.	https://www.hkl-xray.com/
HKL3000	HKL Research Inc.	https://www.hkl-xray.com/; RRID: SCR_015023
PHASER	McCoy et al., 2007	https://www.phenix-online.org/; RRID: SCR_014219
Phenix	Adams et al., 2010	https://www.phenix-online.org/; RRID: SCR_014224
Coot	Emsley et al., 2010	https://www2.mrc-lmb.cam.ac.uk/personal/pemsley/coot/; RRID: SCR_014222
MolProbity	Williams et al., 2018	http://molprobity.biochem.duke.edu/; RRID: SCR_014226
PyMOL	DeLano Scientific LLC	http://pymol.sourceforge.net/; RRID: SCR_000305
ASTRA6.1	Wyatt Technology Corporation	https://www.wyatt.com/products/software/astra.html; RRID: SCR_016255
Origin7.0	OriginLab	https://www.originlab.com/; RRID: SCR_002815

RESOURCE AVAILABILITY

Lead Contact

Further information and requests for resources and reagents should be directed to and will be fulfilled by the Lead Contact, Mingjie Zhang (mzhang@ust.hk)

Materials Availability

Materials generated in this study are available upon request from the Lead Contact.

Data and Code Availability

The atomic coordinates of the SAV1 WW12ex structure and the structure of SAV1 WW12 in complex with Dendrin PY23 have been deposited to the Protein Data Bank under the accession codes of 7BQF and 7BQG, respectively.

EXPERIMENTAL MODEL AND SUBJECT DETAILS

Cell lines

HEK293K cells (from ATCC) were maintained in DMEM (GIBCO) containing 10% fetal bovine serum (FBS, GIBCO), 100 U/mL penicillin and 100 mg/mL streptomycin and with 5% CO_2 at 37 °C. Cells were tested using morphology, karyotyping, and PCR-based approaches to confirm their identity. Cells were tested negative for mycoplasma contamination by cytoplasmic DAPI staining.

METHOD DETAILS

Constructs, Protein Expression and Purification

The coding sequence of SAV1 WW12ex was PCR amplified using mouse brain cDNA as template. The rest of the constructs were described in our earlier studies (Ji et al., 2019; Lin et al., 2019). For crystallization, Dendrin (residues P224-G235) was covalently linked to the C terminus of SAV1 WW12 (residues E198-V271) by a two-step PCR method. Various fragments and mutants were created using the standard PCR-based and the standard PCR-based site-directed mutagenesis methods, respectively. All constructs were confirmed by DNA sequencing. All constructs used for protein expression were individually cloned into a pET vector and recombinant proteins

were expressed in Codon-plus BL21 (DE3) *Escherichia coli* cells with induction of protein expression by 0.3 mM IPTG at 16 °C overnight. All recombinant proteins were purified using Ni^{2+}-nitrilotriacetic acid agarose (Ni-NTA) column followed by size exclusion chromatography (Superdex 200 column from GE Healthcare). The tags of the recombinant proteins were removed before crystallization.

Crystallization and Data Collection

The crystals were obtained by hanging drop vapor diffusion method at 16 °C within 3–5 days. Crystals of SAV1 WW12ex were grown in solution containing 2% v/v 1,4-Dioxane, 10%–20% w/v PEG 3350 and 100 mM Tris-HCl (pH 8.0); crystals of SAV1/Dendrin complex were grown in solution containing 4 M Potassium formate, 2% w/v PEG 2000 MME and 100 mM BIS-TRIS propane (pH 9.0). Before diffraction experiments, crystals were soaked in the original crystallization solutions containing an additional 10%–25% glycerol for cryoprotection. All diffraction data were collected at the Shanghai Synchrotron Radiation Facility BL17U1 or BL19U1. Data were processed and scaled by HKL2000 (Otwinowski and Minor, 1997) or HKL3000 (Minor et al., 2006).

Structure Determination and Refinement

The two structures were determined by molecular replacement using PHASER (McCoy et al., 2007). The initial phase of SAV1 WW12ex was solved using the structures of SAV1 WW1 (PDB code: 2YSB) and WW2 (PDB code: 2DWV) as the searching models. The initial phase of the SAV1/Dendrin complex was solved using the WW tandem part from the structure of SAV1 WW12ex. The extension of SAV1 ex and the PY23 motif of Dendrin were manually built according to the F_{obs} - F_{calc} difference Fourier maps in COOT (Emsley et al., 2010). Further manual model adjustment and refinement were completed iteratively using COOT and PHENIX (Adams et al., 2010) based on the $2F_{obs}$ - F_{calc} and F_{obs} - F_{calc} difference Fourier maps. The final models were further validated by MolProbity (Williams et al., 2018). Detailed data collection and refinement statistics are summarized in Table S1. All structure figures were prepared using PyMOL (http://pymol.sourceforge.net/).

Isothermal Titration Calorimetry Assay

Isothermal Titration Calorimetry (ITC) experiments were carried out on a VP-ITC calorimeter (Micro-Cal) at 25 °C. Titration buffer contained 50 mM Tris-HCl (pH 7.8), 100 mM NaCl, 1 mM DTT and 1 mM EDTA. All samples were degassed and cleared by centrifugation before the experiment. For a typical experiment, each titration point was performed by injecting a 10 μL aliquot of a protein sample (300 μM) into the cell containing a reactant (30 μM) at a time interval of 120 s to ensure that the titration peak returned to the baseline. The titration peaks were automatically integrated and normalized by Origin7.0 (MicroCal). Data were fitted using the one-site binding model within the Origin7.0. The dissociation constants are reported as values ± fitting errors.

Analytical Gel Filtration Chromatography Coupled with Static Light Scattering

An AKTA FPLC system (GE Healthcare) equipped with analytical gel filtration column and coupled with static light scattering and differential refractive index detector (miniDawn, Wyatt) was used for the assays. Protein samples (100 μL with the concentration of 25-100 μM) were loaded to a Superose 12 10/300 GL column (GE Healthcare) pre-equilibrated with the assay buffer (same as that used in the ITC experiments). Data were analyzed with ASTRA6 (Wyatt).

Transfection and Lentiviral Infection

Cells were seeded in 6-well plates for 24 hr, and then were transfected with plasmids using PolyJet Reagent (Signagen Laboratories) according to the manufacturer's instruction. To generate HEK293A cells stably expressing Flag-SAV1 WT or mutants (Y273E, S245D, and Y273E/S245D), stable HEK293A cells with SAV1 KO (Plouffe et al., 2016) were individually infected with lentivirus packed with plasmids expressing empty vector (plenti-EF1α), Flag-SAV1, or Flag-SAV1 mutants. Forty-eight hours after infection, cells were selected with 1 μg/mL puromycin (Thermo Fisher) in the culture medium. To stimulate the Hippo pathway, low confluence cells (0.5×10^5 cells per well) in 12-well plates were treated with serum starvation.

Immunoblotting and Immunoprecipitation

Immunoblotting was performed with the standard methods as described (Yu et al., 2012). Antibodies for SAV1 (#13301), LATS1 (#3477), MST1 (#3682), pLATS (#8654S), Myc (#2278) were from Cell Signaling Technology; Anti-Flag antibody (#F1804) was from Sigma-Aldrich; c-*myc* (#sc-789), GAPDH (#sc-25778) were obtained from Santa Cruz Biotechnology. For immunoprecipitation, cells were harvested at 48 hr after transfection with lysis buffer containing 50 mM Tris-HCl (pH 7.5), 150 mM NaCl, 1 mM EDTA, 1% NP-40, 10 mM pyrophosphate, 10 mM glycerophosphate, 50 mM NaF, 1.5 mM Na_3VO_4, protease inhibitor cocktail (Roche), and 1 mM PMSF. After centrifuging at 13,300 × g for 15 min at 4 °C, supernatants were collected for immunoprecipitation. Anti-Myc or Anti-Flag antibody was added to the supernatants and the mixtures were incubated with rotation overnight at 4 °C. Then Pierce Protein A/G Magnetic Beads (Thermo Fisher) were added to the mixtures and further incubated with rotation for 2 hr at 4 °C. Immunoprecipitated proteins were eluted with SDS-PAGE sample buffer, resolved by SDS-PAGE and probed by the indicated antibodies.

QUANTIFICATION AND STATISTICAL ANALYSIS

ITC data were analyzed by Origin7.0 (MicroCal). The dissociation constants are shown as values ± fitting errors.

Cell Reports, Volume *32*

Supplemental Information

A WW Tandem-Mediated Dimerization Mode of SAV1 Essential for Hippo Signaling

Zhijie Lin, Ruiling Xie, Kunliang Guan, and Mingjie Zhang

SUPPLEMENTARY FIGURES AND TABLES

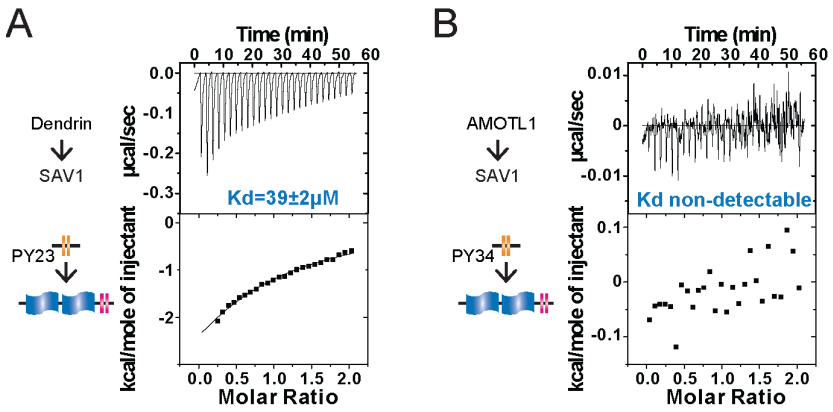

Figure S1. The bindings of SAV1 WW12ex to closely spaced PY-motif repeats from Dendrin and AMOTL1. Related to Figure 1.

(A-B) ITC binding curves showing the bindings of SAV1 WW12ex to PY-motifs from Dendrin (A) and AMOTL1 (B). K_d values of the ITC assays reported in this study are reported as fitted result ± fitting error of the corresponding experimental binding curve.

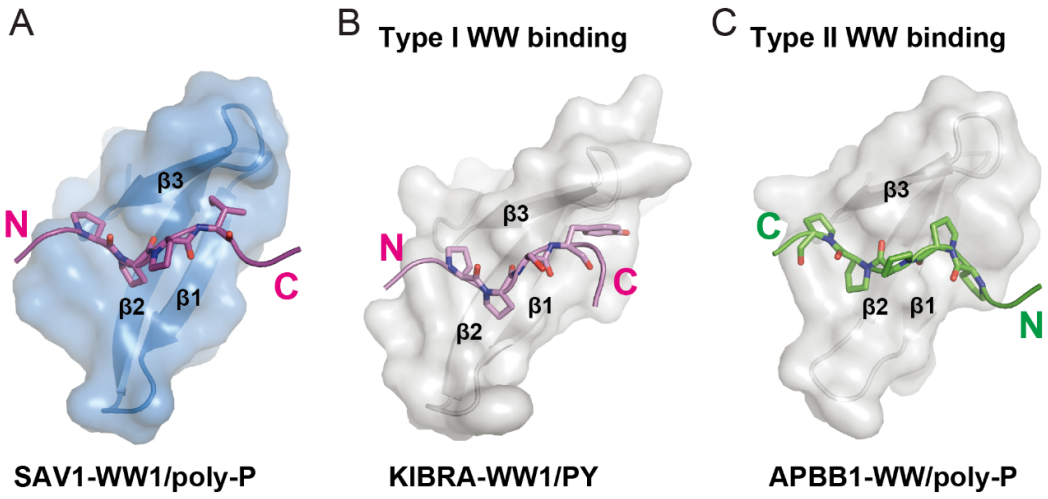

Figure S2. Poly-P motif from SAV1 extension sequence binds to SAV1 WW1 using the type I WW/PY-motif binding mode. Related to Figure 2 and Figure 3. (A-C) Combined surface-ribbon-stick diagram showing the "PPPI"-motif binds to SAV1 WW1 (A), and the examples of the type I (B; PDB code: 6J69) and II (C; PDB code: 2HO2) WW/target binding modes. Note that the orientation of the "PPPI" motif bound to SAV1 WW1 is the same to that of the PY-motif bound to the type I WW domain of KIBRA WW1 but opposite to that of the poly-P motif bound to the type II WW domain from APBB1.

A

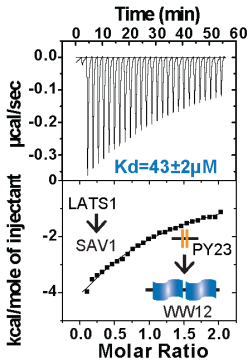

B

LATS1-PY23	WW12 tandem	Kd (µM)	fold
	SAV1	43±2	1
	KIBRA	0.78±0.02*	~1/55
	MAGI1	19±1*	~1/2
	MAGI2	0.65±0.02*	~1/66
	MAGI3	0.47±0.01*	~1/91

Figure S3. ITC experiments showing that SAV1 WW12, compared to WW tandems of KIBRA, MAGI2 and MAGI3, has a much weaker binding to LATS1 PY23. Related to Figure 3.

(A) ITC curve showing the binding of LATS1 PY23 binding to the WW12 tandem of SAV1.

(B) Summary of ITC-derived binding affinities of LATS1 PY23 to the WW tandems of SAV1, KIBRA, MAGI1-3. *Data from our previous study (Lin et al., 2019).

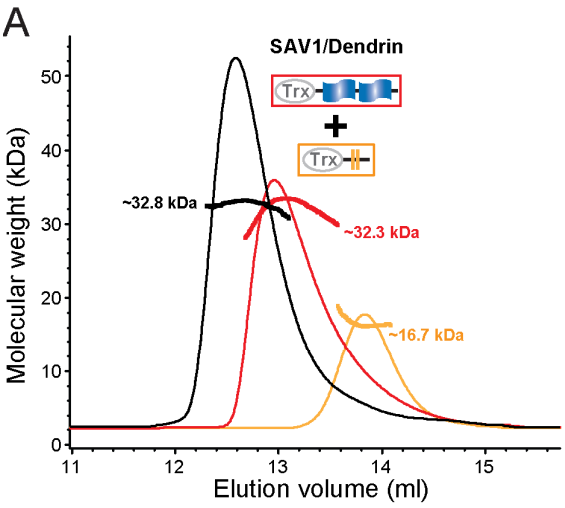

TRX-protein	Theoretical MW for monomeric unit (kDa)	Detected MW (kDa)
Trx	23.0	32.3
Trx	16.6	16.7
1:1 Mixture	39.6	32.8

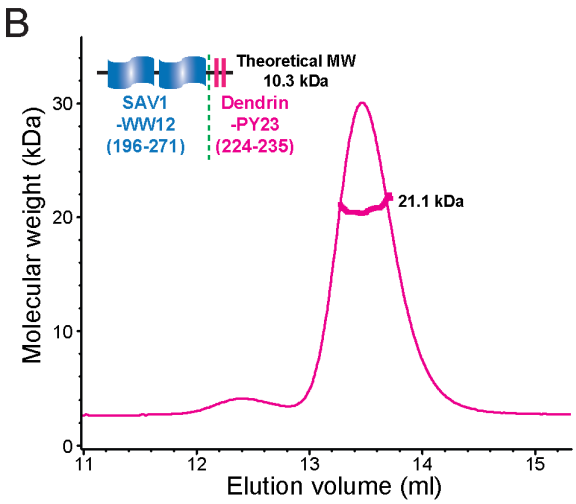

Figure S4. SAV1 WW12 forms a stable complex with Dendrin PY23 in solution. Related to Figure 4.

(A) Analytical gel filtration chromatography coupled with static light scattering analysis showing SAV1 WW12 and Dendrin PY23 form a stable 1:1 complex in solution

(B) Analytical gel filtration chromatography coupled with static light scattering analysis of the fusion protein SAV1 WW12 fused with Dendrin PY23 used for crystallization showing that the fusion protein forms a stable dimer in solution.

A

TRX-SAV1		Theoretical MW for monomeric unit (kDa)	Detected MW (kDa)
WW12ex	WT	~24.9	~45.7
	S245D		~46.0
	Y273E		~29.6
	Y273E/S245D		~24.4
WW12	WT	~23.0	~32.3
	S245D		~22.4

B

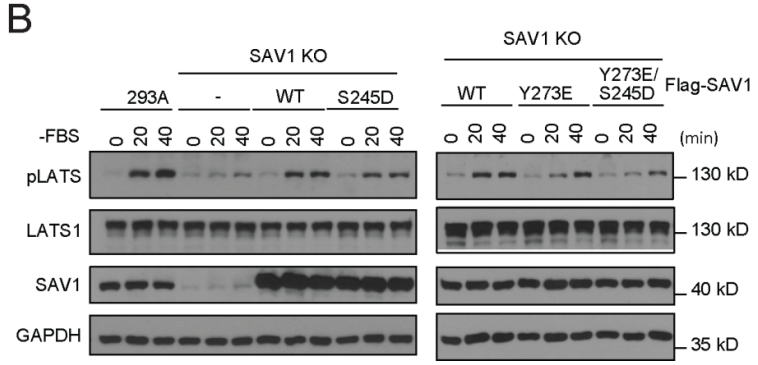

Figure S5. WW12ex mediated SAV1 dimerization is essential for the MST/SAV1 complex assembly upon Hippo activation. Related to Figure 5.

(A) Summary of the dimerization statuses of various forms of WW12ex and WW12 derived from the analytical gel filtration chromatography coupled with static light scattering analyses.

(B) Comparison of LATS1 phosphorylation of HEK293A containing endogenous WT SAV1, SAV1 KO cells, and SAV1 KO cells stably re-expressing WT or mutant SAV1 under the serum starvation condition. SAV1 carrying dimerization defective mutation Y273E (SAV1-Y273E and SAV1-Y273E/S245D) had diminished LATS1 phosphorylation when compared to WT SAV1 and SAV1-S245D.

A

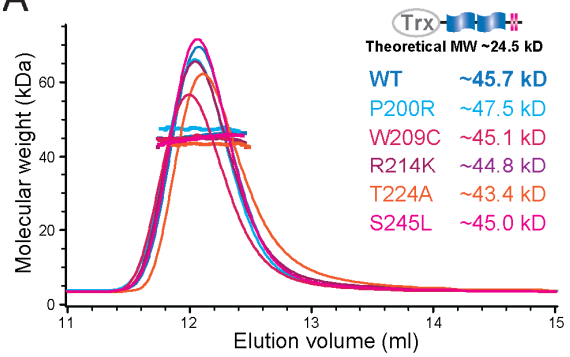

B

WW12	Binding To Dendrin Kd (μM)
WT	**1.7±0.1**
P200R	2.1±0.1
W209C	4.6±0.2
R214K	1.4±0.1
T224A	10±1
R233Q	7.0±0.2
S245L	3.9±0.1
D254H	12±3
Y262H	9.5±0.7

Figure S6. Cancer-derived variants distribute in SAV1 WW12ex. Related to Figure 6.

(A) Analytical gel filtration chromatography coupled with static light scattering analyses of SAV1 WW12ex and its various mutants.

(B) ITC-based measurements comparing the binding affinities of Dendrin PY23 to the WT and various mutants of SAV1 WW12. Pro200 is located outside SAV1 WW12ex, therefore the P200R mutation should not have any impact on the dimer formation of WW12ex. The P200R mutant served as another control similar to the WT WW12ex.

Table S1: Statistics of Data Collection and Model Refinement. Related to Figure 2 and Figure 4.

	WW12PR	WW12/Dendrin
Data collection		
X-ray source	SSRF	SSRF
Space group	$P3_121$	$C222$
Unit cell parameters (Å)	a= b=46.7; c=83.2	a=38.8; b=43.1; c=99.4
Resolution range (Å)	50-1.7(1.73-1.7)	50-1.55(1.58-1.55)
No. of unique reflections	11,842(602)	11,875(599)
Redundancy	18.9(18.3)	12.8(8.6)
I/σ	48.6(3.0)	39.1(2.0)
Completeness (%)	100(100)	99.6(99.3)
R_{merge} (%)[a]	5.3(69.7)	5.8(100)
$CC_{1/2}$(highest-resolution shell)	0.95	0.69
Structure refinement		
Resolution (Å)	50-1.7(1.77-1.7)	50-1.55(1.62-1.55)
R_{cryst}[b] / R_{free}[c]	19.9/22	18.2/21.7
r.m.s.d bonds (Å) / angles (º)	0.007/0.97	0.006/1.0
Average B-factors[d]	36	18
No. of atoms		
Protein atoms	694	716
Water molecules	66	92
Ramachandran plot[d]		
favored regions(%)	100	97.7
allowed regions(%)	0	2.3
outliers(%)	0	0

Numbers in parentheses represent the value for the highest resolution shell.

a. $R_{merge} = \Sigma |I_i - \langle I \rangle| / \Sigma I_i$, where I_i is the intensity of measured reflection and $\langle I \rangle$ is the mean intensity of all symmetry-related reflections.

b. $R_{cryst}=\Sigma||F_{calc}| - |F_{obs}||/\Sigma F_{obs}$, where F_{obs} and F_{calc} are observed and calculated structure factors.

c. $R_{free}= \Sigma_T||F_{calc}| - |F_{obs}||/\Sigma F_{obs}$, where T is a test data set of about 10% of the total unique reflections randomly chosen and set aside prior to refinement.

d. B factors and Ramachandran plot statistics are calculated using MolProbity.